Co-operative Influence of O_2 and H_2O in the Degradation of Layered Black Arsenic

Mayank Tanwar[1+], Sagar Udyavara[1+]*, Hwanhui Yun[1], Supriya Ghosh[1], K. Andre Mkhoyan[1]*, Matthew Neurock[1,2]*

[1]*Department of Chemical Engineering and Materials Science, University of Minnesota, Minneapolis, Minnesota 55455, USA*

[2]*Department of Chemistry, University of Minnesota, Minneapolis, Minnesota 55455, USA*

[+]These authors contributed equally to the work

Corresponding Authors: udyav001@umn.edu (SU), mkhoyan@umn.edu (KAM), mneurock@umn.edu (MN)

Abstract

Layered black arsenic (b-As) has recently emerged as a new anisotropic two-dimensional (2D) semiconducting material with applications in electronic devices. Understanding factors affecting the ambient stability of this material remains crucial for its applications. Herein we use first-principles density functional theory (DFT) calculations to examine the stability of the (010) and (101) surfaces of b-As in the presence of oxygen (O_2) and water (H_2O). We show that the (101) surface of b-As can easily oxidize in presence of O_2. In the presence of moisture contained in air, the oxidized b-As surfaces favorably react with H_2O molecules to volatilize As in the form of $As(OH)_3$ and $AsO(OH)$, which results in the degradation of the b-As surface, predominantly across the (101) surface. These predictions are in good agreement with experimental electron microscopy observations, thus demonstrating the co-operative reactivity of O_2 and H_2O in the degradation of layered b-As under ambient conditions.

Keywords

The examination of two-dimensional (2D) materials has led to many scientific advances and ground breaking applications in the recent past.[1–4] Among the various studied 2D materials, layered black arsenic (b-As) is emerging as a new elemental 2D material from the pnictogen group with characteristic properties comparable to or better than those of black phosphorus (BP).[5–7] Despite being synthesized only recently,[5,6,8,9] b-As has already shown desirable layer-number-dependent electronic properties and the potential for being one of the building block materials for next-generation opto-electronic devices.[6,10,11] A more detailed understanding of black arsenic's ambient stability and establishing ways to improve it, however, are required for its utilization. The study by Yun et al.[12] showed that b-As degrades at atmospheric conditions, and the rate of degradation is sensitive to the humidity of the air. It was observed that, despite structural similarities with BP, b-As degrades primarily by volatilization of As atoms from the surface. Yun et al.[12] also showed that b-As flakes, when kept at elevated humidity, experience strong directional etching along particular crystallographic planes that are perpendicular to its layers. The volatilization of As atoms from b-As structure suggests that during ambient degradation, As likely reacts with O_2 and H_2O molecules present in the surrounding atmosphere to form volatile arsenic species. The observed degradation of b-As is in stark difference with ambient degradation of BP, which is driven mainly by the formation of amorphous P_xO_y.[13–22] Thus, to close the gap in understanding the chemical transformations that lead to b-As degradation at ambient conditions, in this work, we examine in detail the interaction of O_2 and H_2O molecules with the different facets of the b-As and their role in its degradation using first-principles density functional theory (DFT) calculations. We propose a mechanism for surface As removal and degradation of b-As under ambient conditions. The mechanism involves an energetically favorable sequential reaction sequence where O_2 first reacts with As to partially oxidize the As surface. Water then subsequently reacts with the oxidized As surface to form volatile $As(OH)_3$ and $AsO(OH)$ intermediates. The key predictions from this theoretical study are validated by comparing with results from scanning transmission electron microscopy (STEM) measurements, which are also presented and discussed herein.

Results and Discussion

STEM studies of b-As ambient stability show that when thin b-As films are kept under regular ambient conditions or in humid air, it disintegrates (Fig. 1), and this disintegration is facilitated

when the relative humidity of the air is high. The directional etching along specific crystalline planes, perpendicular to layers, appears to be the dominate process (Fig. 1b). While etching along As {201}, {101}, and {102} planes was observed, etching along the {101} plane was the most common.[12] These observations also suggest that when b-As reacts with H_2O and O_2 molecules present in the air, it will result in the formation of As-containing gaseous compounds.
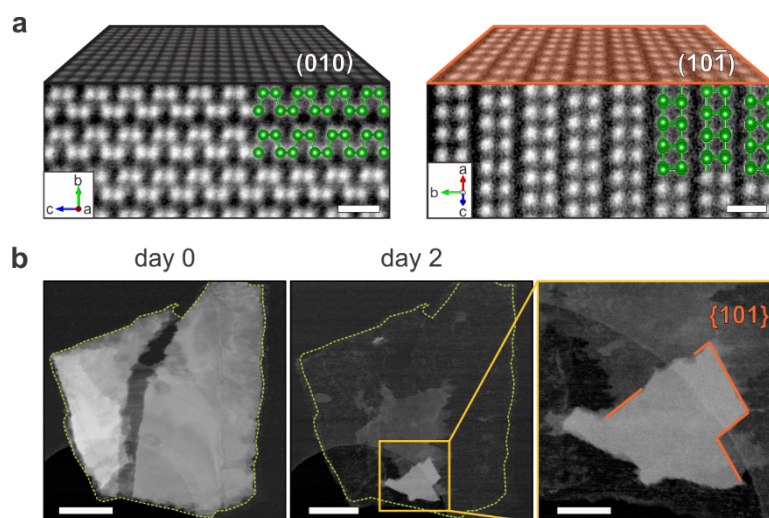

Figure 1. High-angle annular dark-field (HAADF)-STEM images of exfoliated b-As. (a) Structures of the b-As constructed using atomic-resolution HAADF-STEM images viewed along the [010] and [101] crystallographic directions. Van der Waal gaps between layers are visible in both directions. Atomic models are overlaid on the side of the images. Scale bars are 0.4 nm. (b) HAADF-STEM images, taken along the perpendicular to b-As layers (*b*-direction), showing the degradation of a b-As flake: as-prepared (day 0) and after being stored in 98% humid air for two days. The initial shape of the flake is outlined with a dashed line. A small and mostly intact section of the b-As flake shows strong directional etching along {101} crystallographic planes. Scale bars are 400 nm.

To evaluate the reactivity of water and oxygen with b-As, models of the b-As films with different exposed surfaces were constructed using the atomic structure of the bulk b-As crystal.[23] These models were then optimized to their establish their lowest energy configurations using *ab initio* DFT simulations (for details, see SM Fig. S1). These optimized surfaces were subsequently used to determine the adsorption and dissociation energies of water and O_2. Two surface terminations of the b-As crystal that were examined in depth were: the (010) surface, which is parallel to the

van der Waals bonded layers, and the easy-etch (101) surface, which is one of the side surfaces perpendicular to layered (010) surface. It should be noted that in the case of the exposed (101) surface, the presence of dangling covalent bonds resulted in slight changes in the atomic configuration of the surface upon optimization with DFT (for details, see SM, Fig. S1).

To evaluate the adsorption of water on b-As surfaces, H_2O molecules were initially placed at low coverages of $1/8^{th}$ of a surface on the (010) surface and $1/16^{th}$ of a surface on the (101) surface (for details, see SM, Fig. S2), and subsequently optimized to determine their lowest energy configurations. After optimization, the initially bound H_2O molecule tends to move further away from the surfaces with a final As-O distance of 3.23 Å for the (010) and 3.28 Å for the (101) surface (Fig. 2) thus resulting in adsorption energies on the (010) and (101) surfaces of ΔE_{ads} = -16 and -19 kJ/mol, respectively. These slightly exothermic energies, along with large interatomic distances, indicate that water is weakly bound to the surface As atoms through weak long-range interactions. Therefore, the adsorption of water to the surfaces of thin b-As films kept under ambient, or even humid conditions, is not favored, and, as such, the covalent-type interactions between the water molecules and surface As atoms are unlikely.
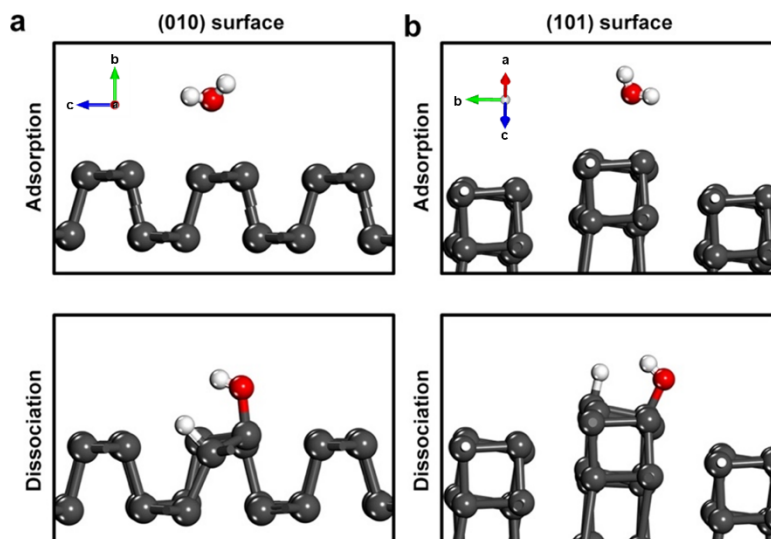

Figure 2. DFT-optimized structures for the adsorption (top) and dissociation (bottom) of H_2O on (a) (010) and (b) (101) surfaces of b-As. In these structures, As atoms are in dark grey color, O in red, and H in white. The adsorption energies and interatomic distances for these structures are reported in Table 1.

The dissociation of a H_2O molecule over two vicinal As atoms on both b-As (010) and (101) surfaces was also considered. Water was found to dissociate over these surfaces resulting in the formation of As-H and As-O(H) bonds with distances of 1.54 and 1.89 Å, respectively, for the (010) surface, and 1.57 and 1.86 Å, respectively for the (101) surface (Fig. 2). The dissociation of H_2O leads to the formation of strong covalent bonds with the surface As atoms (see Table 1), which tend to pull the As atoms away from the surfaces as shown in Fig. 2. The energy for the dissociative adsorption of the H_2O molecule on the b-As surfaces, however, was found to be highly endothermic with dissociation energies as high as ΔE_{diss} = 163 and 101 kJ/mol for (010) and (101) surfaces, respectively, thus making dissociation very unlikely to occur. Therefore, it can be concluded that water alone will not likely react with b-As to cause the experimentally observed degradation.

The role of oxygen in the degradation of b-As was subsequently evaluated by considering the adsorption of O_2 on the (010) and (101) surfaces. Three different modes of adsorption of O_2 over the b-As surfaces were examined: (i) molecular O_2 adsorption via di-σ bonding where the two oxygen atoms of O_2 form covalent bonds to two vicinal surface As atoms; (ii) molecular O_2 adsorption via π-bonding where O_2 binds to a single As atom via a single π-bond; and (iii) dissociative O_2 adsorption over two vicinal surface As atoms. The optimized structures for the dissociative adsorption mode are shown in Fig. 3 and the resulting As-O and O-O distances along with adsorption and dissociative reaction energies are summarized in Table 1(see SM Fig. S3 for di-σ and π-bonding modes of adsorption). The results indicate that only the dissociative O_2 adsorption is exothermic on both surfaces, while the other two modes of molecular absorption are endothermic. It should be noted that, while the gas phase O_2 is in a triplet spin state with two unpaired electrons, the dissociative adsorption of O_2 leads to the formation of two singlet oxygen atoms that covalently bind to As atoms on the surface. The strong covalent bonds that form between the surface As and the O atoms result in the high exothermic reaction energies of ΔE_{diss} = -163 and -164 kJ/mol for the (010) and the (101) surfaces, respectively. Further evaluation of the transition states and activation energies for O_2 dissociation show a higher barrier of 76 kJ/mol for dissociation over the (010) surface and a much lower barrier of 17 kJ/mol for dissociation over the (101) surface (Fig. S5(b)). This can be attributed to dissociation over the saturated rigid

6

framework of the (010) surface as compared to the reconstructed (101) surface which initially had unsaturated dangling bonds prior to reconstruction. The low barriers observed over the (101) surface compared to (010) surface suggests that the (101) surfaces will be more easily oxidized compared to the relatively more stable (010) surface which, as we shall see in the succeeding sections, leads to preferential degradation along the (101) plane. Thus, it can be speculated that if the b-As films are kept at ambient conditions with oxygen in the air, the exposed surfaces will begin to oxidize predominantly via O_2 dissociation over the (101) surface.
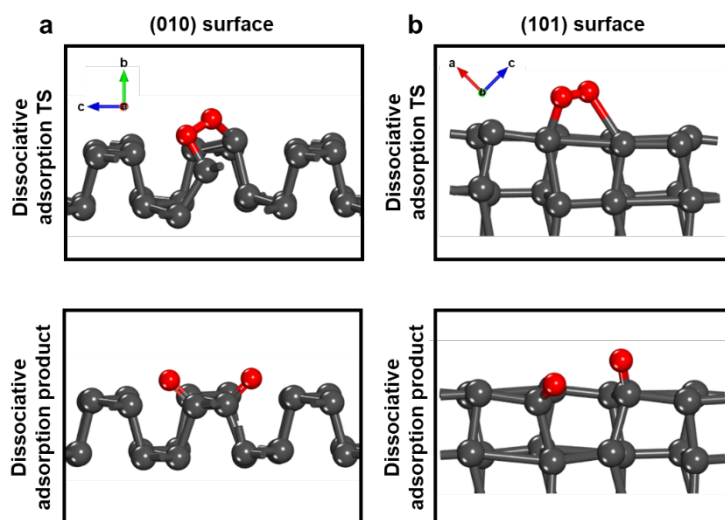

Figure 3. DFT-optimized transition (top) and product state (bottom) structures for dissociative O_2 adsorption on (a) (010) and (b) (101) surfaces of b-As. The dissociative reaction energies and activation barriers along with the reaction energies for the other adsorption modes and their respective interatomic distances are listed in Table 1. In these structures, the As atoms are shown in dark grey color, O in red, and H in white.

Table 1. Interatomic distances and the adsorption and dissociative reaction energies for the different O_2/H_2O adsorption and reaction steps that can occur over the (010) and (101) surface terminations of b-As.

Reaction step	Bond	Bond distances (Å)		Adsorption and dissociative reaction energies (kJ/mol)	
		(010)	(101)	(010)	(101)
H_2O adsorption	As-O	3.234	3.283	-16	-19
H_2O dissociation	As_1-H	1.540	1.565	163	101
	As_2-O	1.898	1.864		
O_2 di-σ adsorption	As_1-O_1	2.218	1.952	63	2
	As_2-O_2	2.225	2.024		
	O_1-O_2	1.350	1.446		
O_2 π-adsorption	As-O_1	1.914	1.908	51	20
	As-O_2	1.832	1.826		
	O_1-O_2	1.573	1.560		
O_2 dissociative adsorption	As_1-O_1	1.692	1.675	-163	-164
	As_2-O_2	1.692	1.669		
O_2 dissociative adsorption TS	As_1-O_1	1.871	2.041	76	17
	As_2-O_2	1.977	2.804		
	O_1-O_2	1.503	1.337		

The dissociative adsorption of oxygen results in the formation of the more active b-A sites on the As surface that may work together to drive the heterolytic dissociation of water. We therefore examined the adsorption of water and its dissociation on the partially oxidized b-As surfaces. The adsorption of H_2O on the partially oxidized As sites was examined on the b-As surfaces with

dissociated O_2 (1/4th of a surface O* coverage on the (010) surface and 1/8th of a surface O* coverage on the (101) surface). Interestingly, similar to the molecular H_2O adsorption on a bare As surface, the optimized structures showed no tendency for H_2O to molecularly adsorb on the oxidized surface as water moves away from the surface (see SM, Fig. S4).

However, when one considers the dissociative adsorption of H_2O onto the partially oxidized b-As surface (for details, see SM discussion and Fig. S5), the adsorption becomes more favorable where the controlling reaction energies depend on the surface termination (Fig. 4). The dissociation of H_2O was calculated to be slightly endothermic for the (010) surface of b-As with a relatively higher barrier (ΔE_{diss} = 5 kJ/mol, $\Delta E^{\ddagger}$ = 12 kJ/mol) whereas the dissociation over the (101) surface was calculated to be exothermic with an overall dissociation energy of ΔE_{diss} = -125 kJ/mol and no activation barrier. The water binds and heterolytically dissociates over two As(O)-As(O) vicinal sites on the surface to form an As(OH)-As(O)(OH) surface intermediate as shown in Fig. 4. Interestingly, the barriers to dissociate water over a single As(O) site are higher than over two As(O)-As(O) vicinal sites for both surfaces (for details, see SM, discussion and Figs. S5).

The adsorption and dissociation of a second H_2O molecule at the As(OH)-As(O)(OH) site to form an As(OH)$_3$ species was calculated to be highly exothermic on both surfaces: ΔE_{diss} = -122 kJ/mol for the (010) surface, and ΔE_{diss} = -70 kJ/mol for the (101) surface, but proceeded with a higher barrier of $\Delta E^{\ddagger}$ = 54 kJ/mol for the (010) surface, and a relatively lower barrier of $\Delta E^{\ddagger}$ = 35 kJ/mol for the (101) surface. The As(OH)$_3$ species that forms is stable and ultimately desorbs from the b-As surfaces leaving behind a vacant site (Fig. 4). This 3-step reaction process, which first includes the dissociation of O_2 and subsequent dissociation of two H_2O molecules on two vicinal As surface sites, is both kinetically as well as thermodynamically favorable over the (101) surface as compared to the (010) surface and thus likely leads to degradation of the b-As films observed in STEM experiments (Fig. 1).
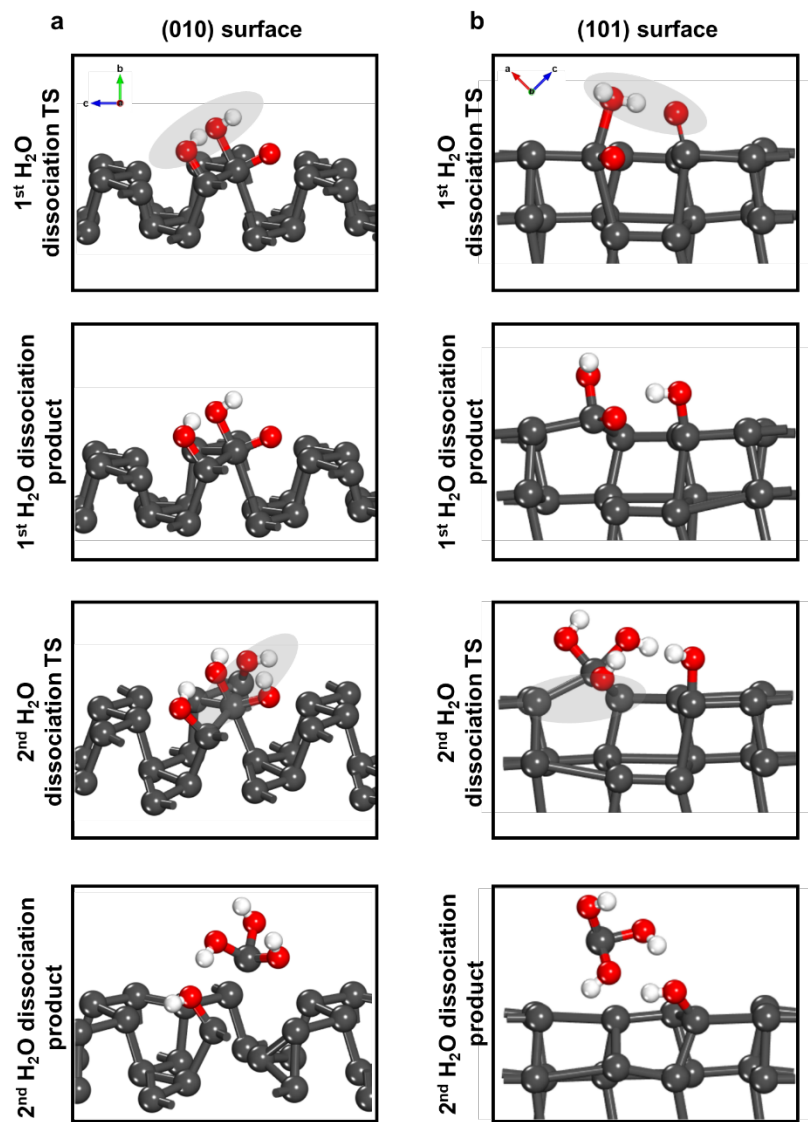
Figure 4. DFT-optimized transition and product state structures for dissociation of the 1st and 2nd H_2O molecule at the oxidized (a) (010) and (b) (101) b-As surfaces resulting in volatilization of As atom as $As(OH)_3$ molecule. The highlighted grey regions corresponds to bond making and breaking in the transition structures. In these structures, As atoms are in dark grey color, O in red, and H in white.

The formation of $As(OH)_3$ and its removal from the b-As surfaces creates a vacancy on the film surface. Since each As is coordinated to three other As atoms, this vacancy gives rise to three unsaturated As atoms. In addition, vacancies on the b-As surface are also expected to be present

due to the finite ambient temperature and surface distortions, which may affect the stability of the surface. As such, we also evaluated the feasibility for the adsorption and dissociation of O_2 and H_2O molecules around a vacancy site over both (010) and (101) b-As surfaces. Since each As atom is initially covalently bonded to three other As atoms, three dangling unsaturated As atoms are present at the vacancy. The relaxation of these resulting surfaces resulted in the reconstruction of the (101) surface where two of these unsaturated As atoms recombine, still leaving one unsaturated As atom as shown in Fig. 5 (for details, see SM Fig. S6). No such surface reconstruction was observed for the (010) surface, leaving all three As atoms uncoordinated.
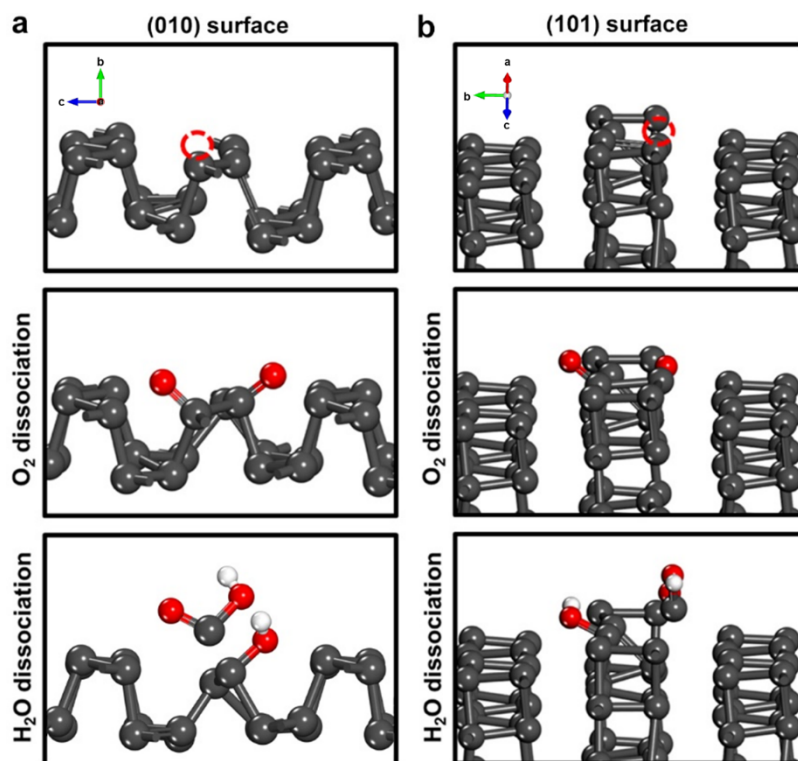

Figure 5: DFT-optimized structures for the (010) and (101) b-As surfaces showing a vacancy on the surface (top, the missing site is highlighted with a red dotted circle), dissociation of O_2 (center) and the first water molecule (bottom) at the As sites adjacent to the vacancy on the (a) (010) and (b) (101) b-As surfaces resulting in volatilization of an As atom as AsO(OH) molecule. In these structures, As atoms are in dark grey color, O in red, and H in white.

The computational results for the adsorption and dissociation of water at an As site adjacent to the vacancy showed that adsorption and dissociation at this site was unlikely. This is similar to results on the pristine As surfaces (for details see SM Fig. S7). On the other hand, as with the defect-free As surfaces, the dissociative adsorption of O_2 was calculated to be very favorable with highly exothermic adsorption energies of ΔE_{diss} = -242 kJ/mol for (010) surface and ΔE_{diss} = -227 kJ/mol for (101) surface (Fig. 5) (see also SM Fig. S8). The molecular adsorption of water at these oxidized As sites adjacent to the vacancy was again found to be unfavorable (see SM Fig. S9). The dissociation of water at these oxidized As site adjacent to the vacancy, on the other hand, was calculated to be favorable with dissociation energies of ΔE_{diss} = -57 kJ/mol for (010) surface and ΔE_{diss} = -100 kJ/mol for (101) surface (Fig. 5) (see also SM Fig. S10). Here, an As atom is removed from the surface as AsO(OH) (arsenious acid) that forms upon the dissociation of the first H_2O as shown in Fig. 5. Hence, once the vacancy forms, the disintegration of that surface becomes even more facile. These results thus suggest that the degradation of b-As should be further accelerated in presence of these vacancies.

Fig. 6 summarizes the energy profile for the overall degradation mechanism over the pristine and defective (010) and (101) surfaces. As can be seen from the profile, the initial oxygen dissociation step has the highest activation barrier for the (010) surface and hence is postulated to be limiting the rate of degradation over this surface. While the dissociative adsorption of oxygen is thermodynamically facile over both the (101) and the (010) surfaces, this step is kinetically favored over the (101) surface with a relatively low barrier of 17 kJ/mol compared to 76 kJ/mol over the (010) surface. The subsequent dissociation of the first water molecule is also energetically favorable over the (101) surface with an exothermic reaction energy of -125 kJ/mol and no activation barrier. This is in contrast with the results for the (010) surface, where the dissociation of the first water molecule is slightly endothermic with a dissociation energy of 5 kJ/mol and activation barrier of 12 kJ/mol. While the 2nd water dissociation is more exothermic over the (010) surface (ΔE_{rxn} = -122 kJ/mol) compared to that over the (101) surface (ΔE_{rxn} = -70 kJ/mol), due to the favorability for the initial oxygen dissociation and water dissociation steps, the reaction energy for the overall cycle leading to As removal is significantly more exothermic for the (101) surface (ΔE_{rxn} = -359 kJ/mol) as compared to the (010) surface (ΔE_{rxn} = -280 kJ/mol). This suggests that the subsequent degradation is expected to predominantly proceed across the (101) surface, thus leading to the formation of As-vacancies. The formation of the As-vacancy sites in turn results in

the coordinative unsaturation of the As atoms that are more reactive thus leading to higher exothermic dissociation energies, as shown in Fig. 6, and more facile and faster degradation of the b-As surface. The degradation likely occurs via a layer-by-layer peeling of the As surface wherein the removal of the first As atom is rate-determining. Once the first As atom is removed and a vacancy site is created, the degradation process becomes energetically more favorable and the whole layer can then rapidly disintegrate.
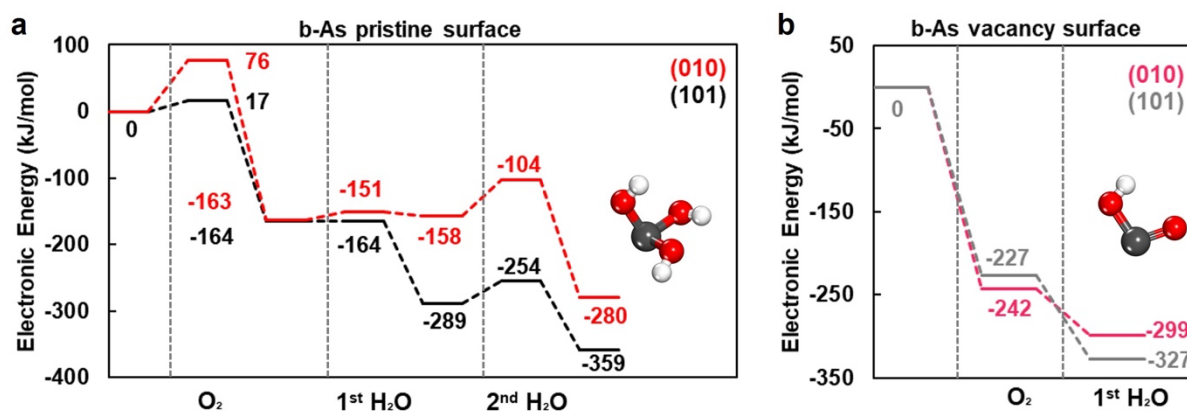

Figure 6. The reaction energy profile comparing the reaction barriers and energies for the dissociation of O_2 and co-dissociation of the first and second H_2O molecules over the (010) surface (red) and the (101) surface (black) of b-As. (a) The 3-step-reaction on the pristine b-As surfaces results in formation of volatile $As(OH)_3$. The reaction energy profile comparing the reaction energies for the dissociation of O_2 and co-dissociation of the first H_2O molecule over the (010) vacancy surface (pink) and the (101) vacancy surface (grey) of b-As. (b) The 2-step-reaction at the surface vacancy site results in formation of volatile $AsO(OH)$.

The predictions from the DFT calculations agree rather well with the experimental observations. When b-As flakes were kept in a dry air environment, with only 1-5 % relative humidity, they only become slightly oxidized without visible changes in flake structure, as shown in Fig. 7(a). This is consistent with the prediction of a favorable exothermic O_2 adsorption on the b-As surfaces with minimal effects on the integrity of the b-As atomic structure. Then, when the b-As flake is exposed to high humidity (98% relative humidity), directional etching across the {101} planes take place also in agreement with the computational results that show the oxygen and water dissociation steps are more facile over the {101} surfaces compared to that over the {010} surfaces. When b-As is

placed in ambient air, under not a particularly high H_2O level, the role of vacancies on the surface degradation becomes important. As seen in Fig. 7(b), b-As flake with defects and vacancies shows that those regions around the surface As-vacancies tend to degrade faster as predicted.
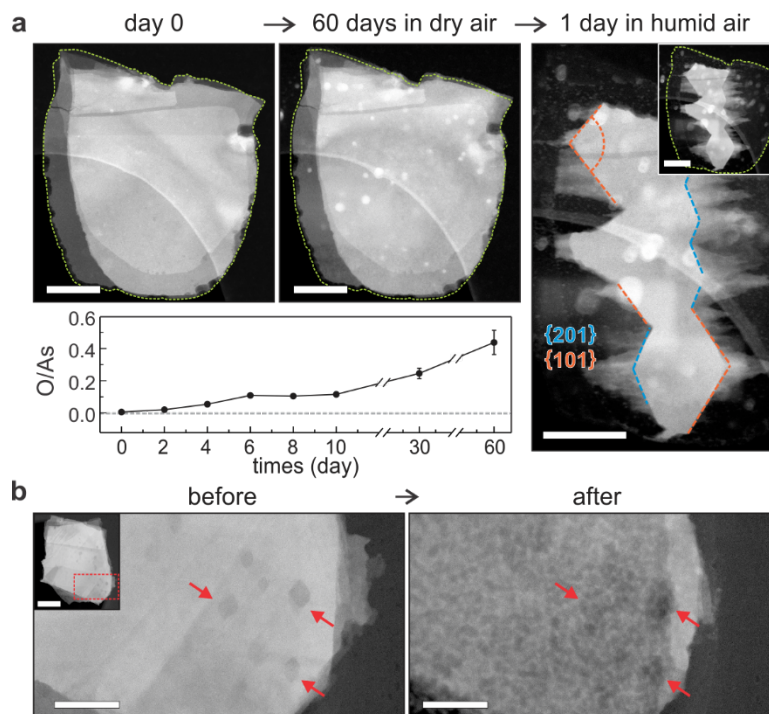

Figure 7. (a) HAADF-STEM images showing the degradation of a b-As flake under different environmental conditions: as-prepared b-As flake (day 0); the b-As flake after stored in dry air for 60 days and after keeping in humid air for one day. The initial shape of the flake is outlined with a dashed line. STEM-EDX compositional analysis shows that when flake is kept in dry air, it accumulates oxygen on its surfaces. All scale bars are 200 nm. (b) HAADF-STEM images of b-As flake showing morphology changes before and after being exposed to ambient air for < 1 hour. Scale bars are 100 nm. Inset image shows the shape of the flake, and the square in the inset indicates the magnified region. Scale bar in the inset is 300 nm. The regions with initial surface damage (indicated with red arrows) have more extended degradation.

In conclusion, while H_2O doesn't seem to react with b-As, in the presence of O_2, it can dissociate and disintegrate b-As. DFT calculations suggest that a plausible mechanism that can result in the degradation of pristine b-As involves three sequential dissociative adsorption steps. The first step involves the rate limiting dissociation of molecular oxygen over vicinal As atoms on the surfaces. A water molecule can then dissociate heterolytically over the As(O)-As(O) surface site to form a surface As(OH)-As(O)(OH) intermediate. A second water molecule can then dissociate

14

heterolytically over this intermediate surface site to form the As(OH)₃ species which subsequently desorbs into the gas phase. The overall degradation process was calculated to be more exothermic for the (101) surface than the (010) surface. In addition, the high activation barrier for the initial oxygen dissociation over the (010) surface limits the initial oxidation and hence the onset of surface degradation. These differences should result in a slow degradation of b-As along the (010) surface compared to the (101) surface. Further, the formation of As-vacancies leads to more favorable and thus faster degradation of the surface via the formation of AsO(OH) species in a two-step-reaction requiring only a single water dissociation. All these predictions are consistent with experimental STEM observations, including that, in absence of water in the air, b-As undergoes surface oxidation with minimal effects on the integrity of the b-As surface structure. The results presented herein describe the critical co-operative role of oxygen and water in degradation of the b-As. It also suggests that keeping the b-As film in an environment where water and O_2 are not present simultaneously will minimize the degradation and dramatically prolong its stability.

Methods

DFT Calculations. All of the calculations described herein were carried out using plane-wave periodic density functional theory (DFT) methods, as implemented in the Vienna *Ab initio* simulation program (VASP).[24–27] The Revised Perdew-Burke-Ernzerhof (RPBE) functional form of the generalized gradient approximation was used along with the Pade Approximation for all of the calculations discussed to determine the corrections to the energy due to exchange and correlation effects.[28] PAW pseudopotentials were used to describe the interactions between the valence and core electrons.[29] D3 dispersion corrections, as proposed by Grimme, were used to account for the long-range interactions present in the system under study.[30] The structures used in the calculations were constructed from the bulk orthorhombic As crystal with lattice constants of a = 3.71 Å, a = 11.44 Å, and c = 4.69 Å.[23] For the (010) surface, the bulk As crystal was cleaved across the (010) plane, and a 2x2 supercell consisting of six layers (or three monolayers) was constructed. An eight-layered (101) surface was similarly constructed with a supercell size of 2×2. A vacuum slab of size 10 Å was inserted between each of these surfaces to avoid spurious interactions across the periodic unit cell along the z-direction (c-axis). The bottom 2 layers of the slab were fixed to their bulk calculated values in all the calculations for both the surfaces. Gamma

centered k-point meshes of 3×3×1and 4×2×1 were used to sample the Brillouin zone (BZ) for the (010) and (101) surface supercells, respectively. The plane waves used in the DFT calculations were constructed using an energy cut-off value of 400 eV. The tolerance for the energy convergence in the SCF cycle was set to 10^{-6} eV. The geometric relaxation was carried out until a maximum force of 0.05 eV/atom was reached.

Transition states were determined, herein, by using a two-step approach. The nudged elastic band (NEB) method[31,32] is used in the first step to establish the location of the transitions. The transition state location is subsequently refined in the second step using the dimer method.[33] In the NEB method, a reaction path is initially described by interpolating a series of images along the reaction coordinate joining reactants to products, which are then optimized until the tangential and normal forces were less than 0.08 eV/Å. The highest energy structure along the reaction coordinate was then used as an initial guess for the dimer method to converge the forces to less than 0.05 eV/Å and isolate the transition state. Spin polarized calculations using ISPIN = 2 tag were performed in the NEB and DIMER calculations for O_2 adsorption and dissociation to account for the triplet nature of O_2 in the gas phase which then forms singlet oxygen atoms on the surface upon dissociation.

STEM Measurements. STEM experiments were performed using aberration-corrected FEI Titan G2 60-300 (S)TEM operated at 200 keV beam energy. HAADF-STEM imaging was carried out using a beam current of ~30 pA and probe convergence angle of 17.2 mrad. ADF detector inner and outer angles for HAADF-STEM imaging were 55 and 200 mrad, correspondingly. b-As flakes used in this study were prepared from b-As crystal purchased from 2D Semiconductors Inc. Plan-view TEM samples were prepared by mechanically exfoliating bulk b-As. The detailed description of TEM sample preparation is reported in Yun et al.[12] The humid air-conditioned and dry air-conditioned samples were stored under an ambient pressure of 760 torr and temperature of 20 ± 0.2 °C. The humidity level was controlled by locating deionized water and desiccants (Calcium sulfate from Sigma-Aldrich) alongside each sample in a closed-glass chamber for humid and dry conditions, respectively. Humidity and temperature of the closed-glass chamber were continuously measured with relative humidity maintained at 96–100 % for humid and 0.6–5 % for dry conditions.

Acknowledgements

Associated content

Author Contributions

SU, KAM, and MN conceived and designed the project. MT performed the DFT calculations with inputs from SU and MN. HY and SG carried out sample preparation, and HY performed STEM experiments and data analysis with inputs from KAM. MT, SU, KAM, and MN analyzed the results of calculations and wrote the manuscript with contributions from all authors.

Supporting Information Available

Optimization of (010) and (101) b-As surfaces, guess structures for molecular water adsorption on the (010) and (101) b-As surfaces, di-σ adsorption and π-adsorption of O_2 on (010) and (101) b-As surface, molecular water adsorption on the oxidized (010) and (101) b-As surfaces, discussion on configurational sampling for the dissociation of water over the oxidized As surfaces, flow diagrams of possible mechanistic routes for oxygen and two water molecules dissociation over the (010) and (101) b-As surfaces, optimization of (010) and (101) b-As surfaces with As vacancy, adsorption and dissociation of the H_2O molecule on (010) and (101) b-As surfaces with As vacancy, di-σ adsorption and π-adsorption of O_2 and H_2O on (010) and (101) b-As surface with As vacancy. This material is available free of charge via the Internet at http://pubs.acs.org.

References

(1)   Nicolosi, V.; Chhowalla, M.; Kanatzidis, M. G.; Strano, M. S.; Coleman, J. N. Liquid Exfoliation of Layered Materials. *Science* **2013**, *340* (6139), 72–75.

(2)   Hu, Z.; Niu, T.; Guo, R.; Zhang, J.; Lai, M.; He, J.; Wang, L.; Chen, W. Two-Dimensional Black Phosphorus: Its Fabrication, Functionalization and Applications. *Nanoscale* **2018**, *10* (46), 21575–21603.

(3)   Xu, Y.; Shi, Z.; Shi, X.; Zhang, K.; Zhang, H. Recent Progress in Black Phosphorus and Black-Phosphorus-Analogue Materials: Properties, Synthesis and Applications. *Nanoscale* **2019**, *11* (31), 14491–14527.

(4)   Wang, Y.; Kim, J. C.; Wu, R. J.; Martinez, J.; Song, X.; Yang, J.; Zhao, F.; Mkhoyan, A.; Jeong, H. Y.; Chhowalla, M. Van Der Waals Contacts between Three-Dimensional Metals and Two-Dimensional Semiconductors. *Nature* **2019**, *568* (7750), 70–74.

(5)   Chen, Y.; Chen, C.; Kealhofer, R.; Liu, H.; Yuan, Z.; Jiang, L.; Suh, J.; Park, J.; Ko, C.; Choe, H. S.; et al. Black Arsenic: A Layered Semiconductor with Extreme In-Plane Anisotropy. *Adv. Mater.* **2018**, *30* (30), 1800754.

(6)   Zhong, M.; Xia, Q.; Pan, L.; Liu, Y.; Chen, Y.; Deng, H. X.; Li, J.; Wei, Z. Thickness-Dependent Carrier Transport Characteristics of a New 2D Elemental Semiconductor: Black Arsenic. *Adv. Funct. Mater.* **2018**, *28* (43), 1802581.

(7)   Kandemir, A.; Iyikanat, F.; Sahin, H. Monitoring the Crystal Orientation of Black-Arsenic: Via Vibrational Spectra. *J. Mater. Chem. C* **2019**, *7* (5), 1228–1236.

(8)   Osters, O.; Nilges, T.; Bachhuber, F.; Pielnhofer, F.; Weihrich, R.; Schöneich, M.; Schmidt, P. Synthesis and Identification of Metastable Compounds: Black Arsenic - Science or Fiction? *Angew. Chemie - Int. Ed.* **2012**, *51* (12), 2994–2997.

(9)   Antonatos, N.; Luxa, J.; Sturala, J.; Sofer, Z. Black Arsenic: A New Synthetic Method by Catalytic Crystallization of Arsenic Glass. *Nanoscale* **2020**, *12* (9), 5397–5401.

(10)   Golani, P.; Yun, H.; Ghosh, S.; Wen, J.; Mkhoyan, K. A.; Koester, S. J. Ambipolar Transport in van Der Waals Black Arsenic Field Effect Transistors. *Nanotechnology* **2020**, *31*, 405203.

(11)   Kundu, S.; Golani, P.; Yun, H.; Guo, S.; Youssef, K. M.; Koester, S. J.; Mkhoyan, K. A. Tunable Metal Contacts at Layered Black-Arsenic/Metal Interface Forming during Metal Deposition for Device Fabrication. *Commun. Mater.* **2022**, *3* (1), 11.

(12)   Yun, H.; Ghosh, S.; Golani, P.; Koester, S. J.; Mkhoyan, K. A. Layer Dependence of

Dielectric Response and Water-Enhanced Ambient Degradation of Highly Anisotropic Black As. *ACS Nano* **2020**, *14* (5), 5988–5997.

(13) Wood, J. D.; Wells, S. A.; Jariwala, D.; Chen, K. S.; Cho, E.; Sangwan, V. K.; Liu, X.; Lauhon, L. J.; Marks, T. J.; Hersam, M. C. Effective Passivation of Exfoliated Black Phosphorus Transistors against Ambient Degradation. *Nano Lett.* **2014**, *14* (12), 6964–6970.

(14) Island, J. O.; Steele, G. A.; Van Der Zant, H. S. J.; Castellanos-Gomez, A. Environmental Instability of Few-Layer Black Phosphorus. *2D Mater.* **2015**, *2* (1), 011002.

(15) Edmonds, M. T.; Tadich, A.; Carvalho, A.; Ziletti, A.; O'Donnell, K. M.; Koenig, S. P.; Coker, D. F.; Özyilmaz, B.; Neto, A. H. C.; Fuhrer, M. S. Creating a Stable Oxide at the Surface of Black Phosphorus. *ACS Appl. Mater. Interfaces* **2015**, *7* (27), 14557–14562.

(16) Favron, A.; Gaufrès, E.; Fossard, F.; Phaneuf-Laheureux, A. L.; Tang, N. Y. W.; Lévesque, P. L.; Loiseau, A.; Leonelli, R.; Francoeur, S.; Martel, R. Photooxidation and Quantum Confinement Effects in Exfoliated Black Phosphorus. *Nat. Mater.* **2015**, *14* (8), 826–832.

(17) Wu, R. J.; Topsakal, M.; Low, T.; Robbins, M. C.; Haratipour, N.; Jeong, J. S.; Wentzcovitch, R. M.; Koester, S. J.; Mkhoyan, K. A. Atomic and Electronic Structure of Exfoliated Black Phosphorus. *J. Vac. Sci. Technol. A Vacuum, Surfaces, Film.* **2015**, *33* (6), 060604.

(18) Pei, J.; Gai, X.; Yang, J.; Wang, X.; Yu, Z.; Choi, D. Y.; Luther-Davies, B.; Lu, Y. Producing Air-Stable Monolayers of Phosphorene and Their Defect Engineering. *Nat. Commun.* **2016**, *7*, 10450.

(19) Luo, W.; Zemlyanov, D. Y.; Milligan, C. A.; Du, Y.; Yang, L.; Wu, Y.; Ye, P. D. Surface Chemistry of Black Phosphorus under a Controlled Oxidative Environment. *Nanotechnology* **2016**, *27*, 434002.

(20) Gamage, S.; Li, Z.; Yakovlev, V. S.; Lewis, C.; Wang, H.; Cronin, S. B.; Abate, Y. Nanoscopy of Black Phosphorus Degradation. *Adv. Mater. Interfaces* **2016**, *3* (12), 1600121.

(21) Walia, S.; Sabri, Y.; Ahmed, T.; Field, M. R.; Ramanathan, R.; Arash, A.; Bhargava, S. K.; Sriram, S.; Bhaskaran, M.; Bansal, V.; et al. Defining the Role of Humidity in the Ambient Degradation of Few-Layer Black Phosphorus. *2D Mater.* **2017**, *4*, 015025.

(22) Liu, P.; Qin, R.; Fu, G.; Zheng, N. Surface Coordination Chemistry of Metal Nanomaterials. *J. Am. Chem. Soc.* **2017**, *139* (6), 2122–2131.

(23) Jain, A.; Ong, S. P.; Hautier, G.; Chen, W.; Richards, W. D.; Dacek, S.; Cholia, S.; Gunter,

D.; Skinner, D.; Ceder, G.; et al. Commentary: The Materials Project: A Materials Genome Approach to Accelerating Materials Innovation. *APL Mater.* **2013**, *1*, 011002.

(24)　Kresse, G.; Hafner, J. Ab Initio Molecular Dynamics for Liquid Metals. *Phys. Rev. B* **1993**, *47* (1), 558–561.

(25)　Kresse, G.; Hafner, J. Ab Initio Molecular-Dynamics Simulation of the Liquid-Metal–Amorphous-Semiconductor Transition in Germanium. *Phys. Rev. B* **1994**, *49* (20), 14251–14269.

(26)　Kresse, G.; Furthmüller, J. Efficient Iterative Schemes for Ab Initio Total-Energy Calculations Using a Plane-Wave Basis Set. *Phys. Rev. B* **1996**, *54* (16), 11169–11186.

(27)　Kresse, G.; Furthmüller, J. Efficiency of Ab-Initio Total Energy Calculations for Metals and Semiconductors Using a Plane-Wave Basis Set. *Comput. Mater. Sci.* **1996**, *6*, 15–50.

(28)　Hammer, B.; Hansen, L. B.; Nørskov, J. K. Improved Adsorption Energetics within Density-Functional Theory Using Revised Perdew-Burke-Ernzerhof Functionals. *Phys. Rev. B - Condens. Matter Mater. Phys.* **1999**, *59* (11), 7413–7421.

(29)　Kresse, G. From Ultrasoft Pseudopotentials to the Projector Augmented-Wave Method. *Phys. Rev. B* **1999**, *59* (3), 1758–1775.

(30)　Grimme, S.; Antony, J.; Ehrlich, S.; Krieg, H.; Grimme, S.; Antony, J.; Ehrlich, S.; Krieg, H. A Consistent and Accurate Ab Initio Parametrization of Density Functional Dispersion Correction (DFT-D) for the 94 Elements H-Pu. *J. Chem. Phys.* **2010**, *132*, 154104.

(31)　Henkelman, G.; Jónsson, H. Improved Tangent Estimate in the Nudged Elastic Band Method for Finding Minimum Energy Paths and Saddle Points. *J. Chem. Phys.* **2000**, *113* (22), 9978–9985.

(32)　Henkelman, G.; Uberuaga, B. P.; Jónsson, H. Climbing Image Nudged Elastic Band Method for Finding Saddle Points and Minimum Energy Paths. *J. Chem. Phys.* **2000**, *113* (22), 9901–9904.

(33)　Henkelman, G.; Jónsson, H. A Dimer Method for Finding Saddle Points on High Dimensional Potential Surfaces Using Only First Derivatives. *J. Chem. Phys.* **1999**, *111* (15), 7010–7022.